

EFFECT OF MOMENTUM CORRELATIONS ON THE PROPERTIES OF FRAGMENTS PRODUCED IN HEAVY-ION COLLISIONS

S. GAUTAM,¹ R. KANT²

¹Department of Physics, Panjab University
(Chandigarh 160 014, India; e-mail: sakshigautam@gmail.com)

²House no. 276, Ward no. 11, Tibbabasti, Patran
(Distt. Patiala-147105, Punjab, India)

PACS 25.70.Pq
©2012

We study the effect of momentum correlations on the properties of light and medium mass fragments by imposing the momentum cut in clustering the phase space. The rapidity distributions, $dN/p_t dp_t$ spectra, and ratio of transverse to longitudinal energy (E_{rat}) for the reactions of $^{12}\text{C}+^{12}\text{C}$ and $^{40}\text{Ca}+^{40}\text{Ca}$ are analyzed. We have found a significant influence of the momentum cut on these properties of the fragments. The results of our calculations are compared with experimental data.

work, we studied the influence of the momentum cut on a fragment structure [6]. We also studied the dependence of the fragmentation on a collision geometry, when the momentum cut is imposed. No study exists in the literature to see the effect of the momentum cut on the various fragment properties like the rapidity distribution, p_t spectra, and E_{rat} . Here, we will see the influence of the momentum cut on various fragment properties and will investigate how these properties depend on the impact parameter within the QMD model [2] described in the following section.

1. Introduction

Intermediate-energy heavy-ion collisions produce a rich amount of information on correlations and fluctuations and eventually on the dynamics and interactions among the nucleons. The breaking of nuclei, i.e., multifragmentation, is one of the rare phenomena that has attracted the major attention in recent years [1]. The physics behind the multifragmentation is so complicated that many different theoretical approaches have been developed [1–3]. Since no theoretical model simulates fragments, one needs afterburners to identify clusters. Since correlations and fluctuations are the main features of the molecular dynamics model, the quantum molecular dynamics (QMD) model is very successful in explaining the phenomenon of multifragmentation. Once the phase space is accessible, one generally clusterizes the phase space with a simple spatial correlation method, where one binds the nucleons in a fragment that lies within a distance of 4 fm. This method is known as the minimum spanning tree (MST) method [4]. At the same time, the fragments formed in the MST method will be highly unstable (especially in central collisions). So, in order to be close to the reality and to filter out such unstable fragments, we impose another cut in terms of the relative momentum of nucleons. This method dubbed as the minimum spanning tree with momentum cut (MSTP) method was discussed by Kumar *et al.* [5]. In our recent

2. The Formalism

2.1. QMD model

We describe the time evolution of a heavy-ion reaction within the QMD model [2], which is based on a molecular dynamics picture. This model has been successful in explaining the collective flow [7], elliptic flow [8], multifragmentation [9], as well as dense and hot matter [10]. In the QMD model, nucleons (represented by Gaussian wave packets) interact via mutual two- and three-body interactions. Here, each nucleon is represented by a coherent state of the form

$$\begin{aligned} \psi_i(\mathbf{r}, \mathbf{p}_i(t), \mathbf{r}_i(t)) &= \\ &= \frac{1}{(2\pi L)^{3/4}} \exp \left[\frac{i}{\hbar} \mathbf{p}_i(t) \times \mathbf{r} - \frac{(\mathbf{r} - \mathbf{r}_i(t))^2}{4L} \right], \end{aligned} \quad (1)$$

where, L defines the interaction range of particles. The total N -body function is assumed to be a direct product of the coherent states [Eq. (1)]

$$\Phi = \prod_i \psi_i(\mathbf{r}, \mathbf{r}_i, \mathbf{p}_i, t). \quad (2)$$

By doing this, one neglects the antisymmetrization. The Wigner transforms of the coherent states are the Gaussians in the coordinate and momentum spaces. The

Wigner density reads

$$\begin{aligned} f_i(\mathbf{r}, \mathbf{p}, \mathbf{r}_i(t), \mathbf{p}_i(t)) &= \\ &= \frac{1}{(2\pi\hbar)^3} \int e^{-\frac{i}{\hbar} \mathbf{p} \cdot \mathbf{r}_{12}} \psi_i(\mathbf{r} + \frac{\mathbf{r}_{12}}{2}, t) \psi_i^*(\mathbf{r} - \frac{\mathbf{r}_{12}}{2}, t) d^3 r_{12}, \\ &= \frac{1}{(\pi\hbar)^3} e^{-(\mathbf{r}-\mathbf{r}_i(t))^2/2L} e^{-(\mathbf{p}-\mathbf{p}_i(t))^2 2L/\hbar^2}. \end{aligned} \quad (3)$$

Here, $\mathbf{r}_i(t)$ and $\mathbf{p}_i(t)$ define the classical orbit or the center of a Gaussian wave packet in the phase space. The density of the i th particle is

$$\begin{aligned} \rho_i(\mathbf{r}) &= \int f_i(\mathbf{r}, \mathbf{p}, \mathbf{r}_i(t), \mathbf{p}_i(t)) d^3 p, \\ &= \frac{1}{(2\pi L)^{3/2}} e^{-[\mathbf{r}-\mathbf{r}_i(t)]^2/2L}. \end{aligned} \quad (4)$$

The equations of motion for a many-body system are then deduced by means of a generalized variational principle: we start from the action

$$S = \int_{t_1}^{t_2} \mathcal{L}[\Phi, \Phi^*] d\tau, \quad (5)$$

with the Lagrange functional

$$\mathcal{L} = \langle \Phi | i\hbar \frac{d}{dt} - H | \Phi \rangle. \quad (6)$$

The time evolution is obtained by the requirement that the action is stationary under the allowed variation of the wave function, i.e.,

$$\delta S = \delta \int_{t_1}^{t_2} \mathcal{L}[\Phi, \Phi^*] dt = 0. \quad (7)$$

The Hamiltonian H contains a kinetic term and mutual interactions V_{ij} , which can be interpreted as the real part of the Brueckner G matrix supplemented by the Coulomb interaction. The time evolution of the parameters is obtained by the requirement that the action be stationary under an allowed variation of the wave function. This yields an Euler–Lagrange equation for each parameter. We obtain the Euler–Lagrange equation for each parameter λ :

$$\frac{d}{dt} \frac{\partial \mathcal{L}}{\partial \dot{\lambda}} - \frac{\partial \mathcal{L}}{\partial \lambda} = 0. \quad (8)$$

If the true solution of the Schrödinger equation is contained in the restricted set of wave functions $\psi_i(\mathbf{r}, \mathbf{r}_i(t), \mathbf{p}_i(t))$, this variation of the action will give the exact solution of the Schrödinger equation. If the parameter space is too restricted, we obtain the wave function in a restricted parameter space which comes closest to the solution of the Schrödinger equation. For the coherent states and a Hamiltonian of the form $H = \sum_i T_i + \frac{1}{2} \sum_{ij} V_{ij}$ (T_i = kinetic energy, and V_{ij} = potential energy), the Lagrangian and the variation can easily be calculated, and we obtain

$$\mathcal{L} = \sum_i \left[-\dot{\mathbf{r}}_i \mathbf{p}_i - T_i - \frac{1}{2} \sum_{j \neq i} \langle V_{ij} \rangle - \frac{3}{2Lm} \right], \quad (9)$$

$$\dot{\mathbf{r}}_i = \frac{\mathbf{p}_i}{m} + \nabla_{\mathbf{p}_i} \sum_j \langle V_{ij} \rangle = \nabla_{\mathbf{p}_i} \langle H \rangle, \quad (10)$$

$$\dot{\mathbf{p}}_i = -\nabla_{\mathbf{r}_i} \sum_{j \neq i} \langle V_{ij} \rangle = -\nabla_{\mathbf{r}_i} \langle H \rangle, \quad (11)$$

with the centroids \mathbf{p}_i and $\tilde{\mathbf{r}}_i$, and $\tilde{\mathbf{r}}_i = \mathbf{r}_i + \frac{\mathbf{p}_i}{m} t$ and $\langle V_{ij} \rangle = \int d^3 \mathbf{r}_1 d^3 \mathbf{p}_2 \langle \psi_i^* \psi_j^* | V(\mathbf{r}_1, \mathbf{r}_2) | \psi_i \psi_j \rangle$. These equations represent the time evolution and can be solved numerically. Therefore, the variational principle reduces the n -body Schrödinger equation to $6 \times (A_P + A_T)$ time-evolution equations, where A_P and A_T are the masses of the projectile and target nuclei. The equations of motion now have a similar structure like the classical Hamiltonian equations

$$\dot{\mathbf{p}}_i = -\frac{\partial \langle H \rangle}{\partial \mathbf{r}_i}; \quad \dot{\mathbf{r}}_i = \frac{\partial \langle H \rangle}{\partial \mathbf{p}_i}. \quad (12)$$

The expectation value of the total Hamiltonian reads

$$\begin{aligned} \langle H \rangle &= \langle T \rangle + \langle V \rangle = \\ &= \sum_i \frac{\mathbf{p}_i^2}{2m_i} + V^{\text{Skyrme}} + V^{\text{Yuk}} + V^{\text{Coul}}. \end{aligned} \quad (13)$$

Here, V^{Skyrme} , V^{Yuk} , and V^{Coul} are, respectively, the local (two and three-body) Skyrme, Yukawa, and Coulomb potentials. The local Skyrme interaction is written as

$$V^{\text{Skyrme}} = \frac{1}{2!} \sum_{j; i \neq j} V_{ij}^{(2)} + \frac{1}{3!} \sum_{j, k; i \neq j \neq k} V_{ijk}^{(3)}. \quad (14)$$

Here, $V_{ij}^{(2)}$ and $V_{ijk}^{(3)}$ represent, respectively, the two- and three-body interactions. The two-body interactions $V_{ij}^{(2)}$

are obtained by folding the two-body potential with the densities of both nucleons.

$$\sum_{j:i \neq j} V_{ij}^{(2)} = \sum_{j:i \neq j} \int f_i(\mathbf{r}_i, \mathbf{p}_i, t) f_j(\mathbf{r}_j, \mathbf{p}_j, t) V(\mathbf{r}_i, \mathbf{r}_j) \times \\ \times d^3 r_i d^3 r_j d^3 p_i d^3 p_j. \quad (15)$$

The three-body interactions can be calculated as follows:

$$\sum_{j,k:i \neq j \neq k} V_{ijk}^{(3)} = \sum_{j,k:i \neq j \neq k} \int f_i(\mathbf{r}_i, \mathbf{p}_i, t) f_j \times \\ \times (\mathbf{r}_j, \mathbf{p}_j, t) f_k(\mathbf{r}_k, \mathbf{p}_k, t) V(\mathbf{r}_i, \mathbf{r}_j, \mathbf{r}_k) \times \\ \times d^3 r_i d^3 r_j d^3 r_k d^3 p_i d^3 p_j d^3 p_k, \quad (16)$$

where the function $f_i(\mathbf{r}_i, \mathbf{p}_i, t)$ is the same function as $f_i(\mathbf{r}, \mathbf{p}, \mathbf{r}_i(t), \mathbf{p}_i(t))$ defined in Eq. (3), though the arguments are formally different. The finite-range Yukawa (V^{Yuk}) and effective Coulomb potential (V^{Coul}) read

$$V^{\text{Yuk}} = \sum_{j:i \neq j} t_3 \frac{\exp(-|\mathbf{r}_i - \mathbf{r}_j|/\mu)}{|\mathbf{r}_i - \mathbf{r}_j|/\mu}, \quad (17)$$

$$V^{\text{Coul}} = \sum_{j:i \neq j} \frac{Z_{\text{eff}}^2 e^2}{|\mathbf{r}_i - \mathbf{r}_j|}. \quad (18)$$

The Yukawa term (with $t_3 = -6.66$ MeV and $\mu = 1.5$ fm) has been added to improve the surface properties of the interaction, which plays an important role in the multifragmentation. In nuclear matter where the density is constant, the interaction density coincides with the single-particle density, and the two-body Skyrme, as well as Yukawa, interactions are directly proportional to $(\frac{\rho}{\rho_o})$. The three-body part of the Skyrme interaction is proportional to $(\frac{\rho}{\rho_o})^2$. In nuclear matter, the local potential energy has the form

$$V^{\text{Skyrme}} = \frac{\alpha}{2} \left(\frac{\rho}{\rho_o} \right) + \frac{\beta}{\gamma + 1} \left(\frac{\rho}{\rho_o} \right)^2. \quad (19)$$

The above potential has two free (α and β) parameters, which can be fixed by the requirement that, at the normal nuclear matter density, the average binding energy should be -15.75 MeV, and total energy should have a minimum at ρ_o . In order to investigate the influence of

different compressibilities $K [= 9\rho^2 \frac{\partial^2}{\partial \rho^2} (\frac{E}{A})]$, the above potential energy [Eq. (19)] can be generalized to

$$V^{\text{Skyrme}} = \frac{\alpha}{2} \left(\frac{\rho}{\rho_o} \right) + \frac{\beta}{\gamma + 1} \left(\frac{\rho}{\rho_o} \right)^\gamma. \quad (20)$$

This equation leads to the nuclear matter equation of state which connects the pressure and the energy. By varying the parameter γ , one can study different equations of state. Naturally, a larger value of γ leads to a hard equation of state, whereas a smaller value of γ results in a soft equation of state. The relativistic effect plays no role in the low incident energy region of the present interest [11]. The phase space of nucleons is stored at several time steps. The QMD model does not give any information about the fragments observed at the final stage of the reaction. In order to construct the fragments, one needs clusterization algorithms. We will concentrate here on the MST and MSTP methods. According to the MST method [4], two nucleons are allowed to share the same fragment if their centroids are closer than a distance r_{min} ,

$$|\mathbf{r}_i - \mathbf{r}_j| \leq r_{\text{min}}, \quad (21)$$

where \mathbf{r}_i and \mathbf{r}_j are the spatial positions of both nucleons, and r_{min} is taken to be 4 fm. The value of r_{min} reflects the cut-off limit of the interaction between nucleons. It should be noted that the value of r_{min} plays a little role, when the system is dilute, and nucleons are far apart from each other. This range of the clusterization parameter will be different in different physical situations depending on the excitation energy and the density at the freeze-out time. It has been shown in [12] that a realistic value of r_{min} is $3 \text{ fm} \leq r_{\text{min}} \leq 5 \text{ fm}$. So we take $r_{\text{min}} = 4$ fm.

For the MSTP method, we impose an additional cut in the momentum space, i.e., we allow only those nucleons to form a fragment, which satisfy, in addition to equation(21),

$$|\mathbf{p}_i - \mathbf{p}_j| \leq p_{\text{min}}, \quad (22)$$

where $p_{\text{min}} = 150$ MeV/c. The value of $p_{\text{min}} = 150$ MeV/c is the average Fermi momentum of the nucleons bound in a nucleus in its ground state, as obtained from the QMD simulations. While considering the space correlations for the fragment formation, we argued that, at a later stage of the reaction, the correlations in the momentum space do not play any role. This argument is based on the assumption that, at a later stage of the

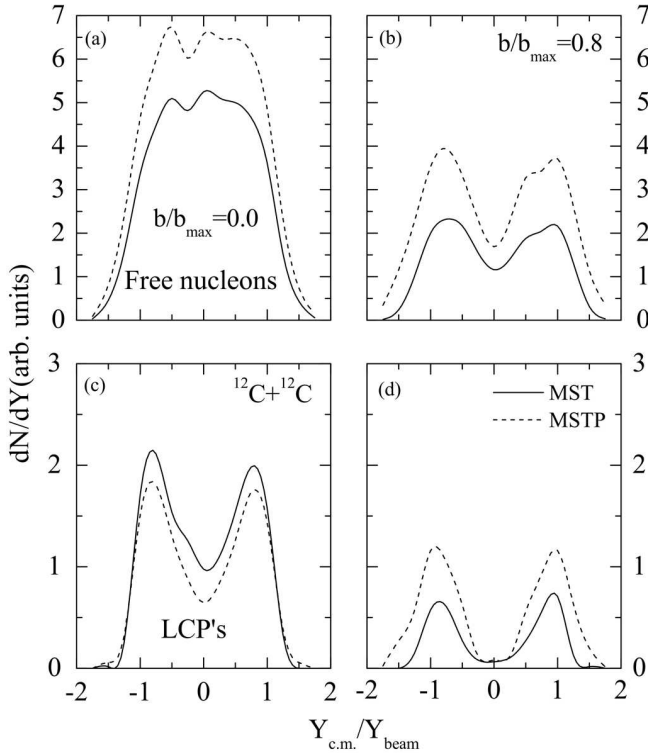


Fig. 1. The rapidity distribution dN/dY vs the rapidity $Y(= Y_{c.m.}/Y_{beam})$ for free nucleons and LCPs for the reaction of $^{12}\text{C}+^{12}\text{C}$ at an incident energy of 100 MeV/nucleon at the central (left panels) and peripheral (right) geometries within the MST and MSTP methods

reaction, the nucleons with large relative momenta dissociate themselves from each other. If we take the value of cut ≈ 150 MeV/c, we find a strong effect of the cut on the fragmentation, as shown in [5]. If we take the value of cut greater than 150 MeV/c, this value is not realistic, as this cut in the relative momentum is too large to keep the nucleons bound in a fragment. If we take p_{min} to be very small, we deny the nucleons to form a fragment even if their relative momentum is small. So the natural choice of the value of cut in the relative momentum of two nucleons is the average Fermi momentum. This means that the nucleons with large relative momentum cannot be in the same fragment, even if they are too close in the coordinate space.

3. Results and Discussion

We simulated the reactions of $^{12}\text{C}+^{12}\text{C}$ and $^{40}\text{Ca}+^{40}\text{Ca}$ at 100 MeV/nucleon at the central and peripheral colliding geometries, i.e., at b (b/b_{max}) = 0.0 and 0.8, respectively, where $b_{max} = R_0(A_P^{1/3} + A_T^{1/3})$, with $R_0 =$

1.142 fm. We use a soft equation of state with the standard energy-dependent Cugnon cross-section.

Figure 1 displays the rapidity distribution vs the rapidity ($Y = Y_{c.m.}/Y_{beam}$), where Y_{beam} is the beam rapidity. We define the rapidity of particles as

$$Y(i) = \frac{1}{2} \ln \frac{\mathbf{E}(i) + \mathbf{p}_z(i)}{\mathbf{E}(i) - \mathbf{p}_z(i)}, \quad (23)$$

where $\mathbf{E}(i)$ and $\mathbf{p}_z(i)$ are, respectively, the total energy and the longitudinal momentum of the i th particle. In Fig. 1, we give the rapidity distribution (dN/dY) of free nucleons and light charged particles ($2 \leq A \leq 4$) (LCPs) for the reaction of $^{12}\text{C}+^{12}\text{C}$ at an energy of 100 MeV/nucleon at the central ($b/b_{max} = 0.0$) (left panels) and peripheral ($b/b_{max} = 0.8$) (right) colliding geometries. The solid and dashed lines indicate the calculations within the MST and MSTP methods, respectively. From the figure, we see that there is a quantitative difference in the results of the MST and MSTP methods, though both methods give qualitatively a similar behavior of the rapidity distribution of nucleons and fragments.

For central collisions (left panels), we see that the peak of the dN/dY plot is pronounced for the MSTP method, which indicates the enhanced production of free nucleons for the MSTP method, as compared to the MST method. This is due to the fact that, in the MST method, we have a single big fragment, because no restriction is imposed on the relative momenta of nucleons forming fragments. In central collisions ($b/b_{max} = 0.0$), the production of LCPs is more within the MST method, as compared to the MSTP method, which is supported by [5, 6]. At the peripheral collisions, the behavior of the rapidity plots of free nucleons is similar to that at the central ones, whereas the trend reverses for the LCPs plot. For LCPs at the peripheral collisions, we have a greater production within the MSTP method. We also see that the dN/dY distribution of free nucleons peaks at a mid-rapidity, by indicating their origin from the participant matter, whereas the peaks at the target and projectile rapidities indicate that IMFs originate from the spectator matter.

In Fig. 2, we show the rapidity distributions of free nucleons, LCPs, and intermediate mass fragments ($5 \leq A \leq A/3$) (IMFs) for the reaction of $^{40}\text{Ca}+^{40}\text{Ca}$. Left (right) panels display the results for $b/b_{max} = 0.0$ (0.8). We find a similar behavior of free nucleons and LCPs, as reported for the reaction of $^{12}\text{C}+^{12}\text{C}$. The IMFs also follow the similar trend as for LCPs, i.e., we have a more (less) production of IMFs within the MST method at the central (peripheral) collisions.

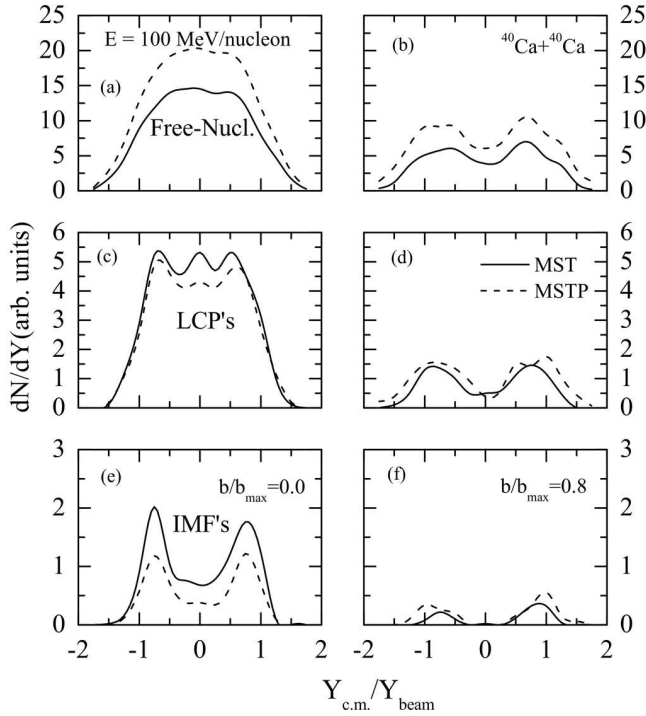


Fig. 2. Same as in Fig. 1, but for the reaction of $^{40}\text{Ca}+^{40}\text{Ca}$

In Figs. 3 and 4, we present $dN/p_t dp_t$ versus p_t for the reactions of $^{12}\text{C}+^{12}\text{C}$ and $^{40}\text{Ca}+^{40}\text{Ca}$, respectively. We see that the $dN/p_t dp_t$ spectra follow the a similar behavior for both MST and MSTP methods. In Fig. 3, we have a higher peak in the spectra of free nucleons within the MST method at both the colliding geometries. The difference between the MST and MSTP methods in the spectra of LCPs is less significant. A similar behavior is also observed for the reaction of $^{40}\text{Ca}+^{40}\text{Ca}$ (see Fig. 4) for free nucleons, LCPs, and IMFs.

In Fig. 5, we display the time evolution of the ratio of transverse to longitudinal energy E_{rat} of free nucleons and LCPs for the reaction of $^{12}\text{C}+^{12}\text{C}$ at the central (left panel) and peripheral (right) colliding geometries. For the MST and MSTP methods, we find a significant difference between the MST and MSTP methods for both free nucleons and LCPs. The difference is more for the central collisions as compared with the peripheral one.

In Fig. 6, we show the time evolution of E_{rat} of free nucleons, LCPs, and IMFs for the reaction of $^{40}\text{Ca}+^{40}\text{Ca}$ at central (left panel) and peripheral (right) collisions. The solid (dashed) lines represent the results of the MST (MSTP) method. From the figure, we find a significant difference of E_{rat} within the MST and MSTP methods, as for the reaction of $^{12}\text{C}+^{12}\text{C}$. We also find that the

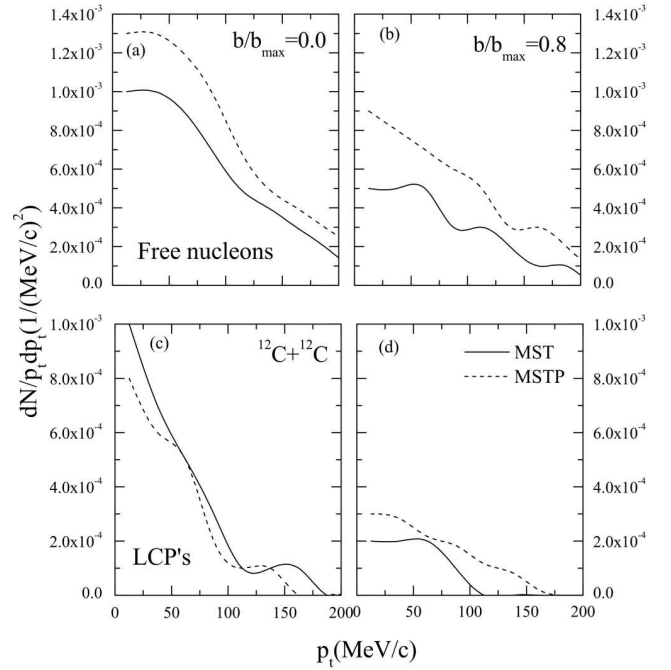


Fig. 3. $\frac{dN}{p_t dp_t} (1/(\text{MeV}/c)^2)$ as a function of the transverse energy p_t for free nucleons and LCPs for the reaction of $^{12}\text{C}+^{12}\text{C}$ at the central (left panels) and peripheral (right) geometries within the MST and MSTP methods. Lines have the same meaning as in Fig. 1

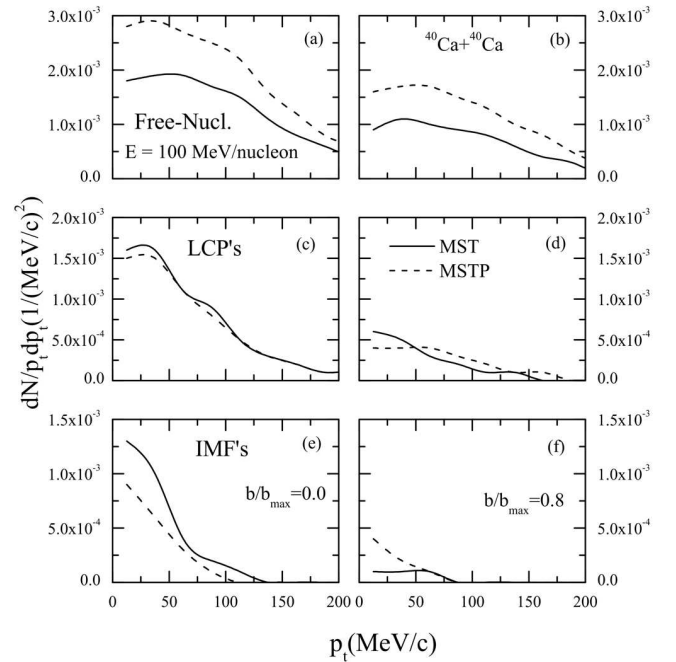


Fig. 4. Same as in Fig. 3, but for the reaction of $^{40}\text{Ca}+^{40}\text{Ca}$

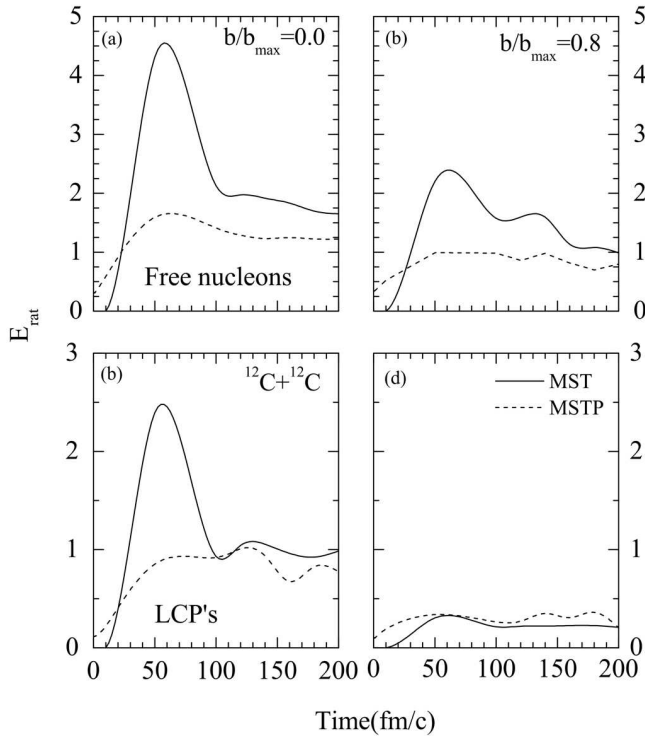


Fig. 5. Time evolution of E_{rat} for free nucleons and LCPs for the reaction of $^{12}\text{C}+^{12}\text{C}$ at central (left panels) and peripheral (right panels) collisions

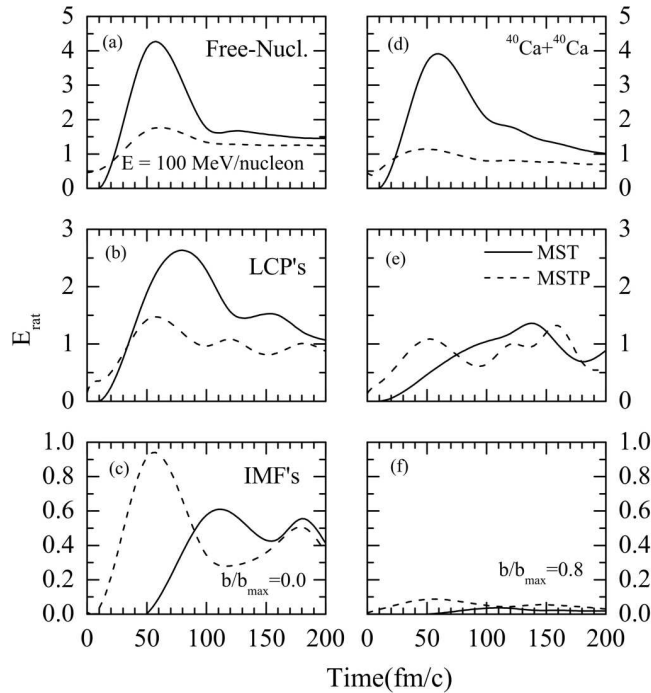


Fig. 6. Same as in Fig. 5, but for the reaction of $^{40}\text{Ca}+^{40}\text{Ca}$

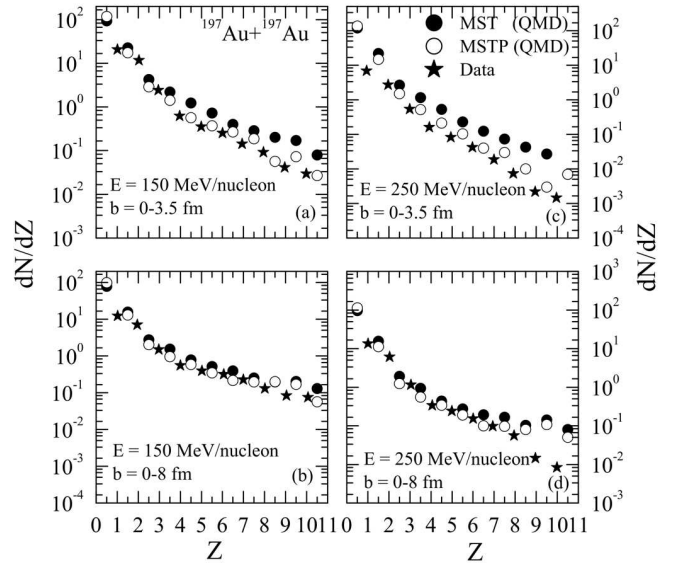


Fig. 7. Charge distribution for central and semicentral collisions of the $^{197}\text{Au}+^{197}\text{Au}$ reactions. The experimental values for central collisions at 150 MeV/nucleon are taken from [13], whereas the ones for semicentral collisions at 150 MeV/nucleon are gathered from [14]. All experimental data for collisions at 250 MeV/nucleon are taken from [15]. Circles represent our theoretical calculations

difference between the MST and MSTP methods reduces at the peripheral colliding geometry.

As a last step, we also compare our results with the experimental data. In Fig. 7, we display the charge distribution for the $^{197}\text{Au}+^{197}\text{Au}$ reaction at 150 (left panels) and 250 (right) MeV/nucleon at the central ($b = 0-3.5$ fm) and semicentral ($b = 0-8$ fm) colliding geometries. The data are taken from [13–15]. Solid (open) circles represent the results for the MST (MSTP) method. From the figure, we see that both MST and MSTP methods obey the qualitative behavior of charge distribution, though, quantitatively, the MST method overestimates the data at both energies and at both colliding geometries. On the other hand, we find that the MSTP method matches the data well at both energies and colliding geometries.

4. Summary

Using the quantum molecular dynamics model, we have studied the effect of momentum correlations on the properties of fragments. This was achieved by imposing a cut in the momentum space during the process of clusterization. The idea of imposing a cut in the momentum space is to avoid the creation of fragments, which are not properly bound and will decay after a while or emit

nucleons in the course of time. By imposing this momentum cut, we have filtered out the unstable fragments, in which nucleons may lie close in the coordinate space, but are far away in the momentum space and hence cannot be a part of the same fragment. Thus, this cut takes us to a more realistic picture. We have shown that this cut on the relative momentum plays a significant role in the rapidity distributions, $dN/p_t dp_t$ spectra, and the E_{rat} behavior of free nucleons, as well as of light and medium mass fragments. Thus, we have found that this cut yields a significant difference in the fragment properties of the system at all colliding geometries. We have also compared our theoretical results with the experimental data, which also signifies the importance of momentum correlations.

The authors are thankful to Dr. Rajeev K. Puri, Department of Physics, Panjab University, Chandigarh, India for valuable discussions. This work has been supported by a grant from Centre of Scientific and Industrial Research (CSIR), Govt. of India.

1. M. Begemann-Blaich, Phys. Rev. C **48**, 610 (1993); M.B. Tsang *et al.*, Phys. Rev. Lett. **71**, 1502 (1993); D.R. Bowmann *et al.*, Phys. Rev. Lett. **67**, 1527 (1991); W. Reisdorf *et al.*, Nucl. Phys. A **612**, 493 (1997); W. Bauer, G.F. Bertsch, and H. Schulz, Phys. Rev. Lett. **69**, 1888 (1992).
2. J. Aichelin, Phys. Rep. **202**, 233 (1991).
3. C. Dorso and J. Randrup, Phys. Lett. B **301**, 328 (1993).
4. S. Kumar *et al.*, Phys. Rev. C **78**, 064602 (2008); G. Batko *et al.*, J. Phys. G: Nucl. Part. Phys. **20**, 461 (1994).
5. S. Kumar and R.K. Puri, Phys. Rev. C **58**, 320 (1998); S.W. Huang *et al.*, Prog. Part. Nucl. Phys. **30**, 105 (2005).
6. S. Gautam and R. Kant, Parmana J. Physics **78**, Iss. 3, 389 (2012).
7. A.D. Sood, R.K. Puri, and J. Aichelin, Phys. Lett. B **594**, 260 (2004); A.D. Sood and R.K. Puri, Eur. Phys. J. A **30**, 571 (2006).
8. S. Kumar *et al.*, Phys. Rev. C **81**, 014601 (2010); *ibid.* C **81**, 014611 (2010).
9. J. Dhawan *et al.*, Phys. Rev. C **74**, 057901 (2006).
10. C. Fuchs *et al.*, J. Phys. G: Nucl. Part. Phys. **22**, 131 (1996); Y.K. Vermani *et al.*, Nucl. Phys. A **847**, 243 (2010).
11. E. Lehmann *et al.*, Phys. Rev. C **51**, 2113 (1995); *ibid.*, Prog. Part. Nucl. Phys. **30**, 219 (1993).
12. J. Singh and R.K. Puri, Phys. Rev. C **62**, 054602 (2000).
13. C. Kuhn, (FOPI collaboration), Phys. Rev. C **48**, 1232 (1993).
14. Th. Wienold, Ph.D. thesis, University of Heidelberg (1993), GSI report, GSI-93-28, ISSN 0171-4546.
15. U. Sodan, Ph.D. thesis, University of Heidelberg (1994).

Received 04.04.11

ВПЛИВ КОРЕЛЯЦІЇ ІМПУЛЬСІВ НА ВЛАСТИВОСТІ ФРАГМЕНТІВ, НАРОДЖЕНИХ У ЗІТКНЕННЯХ ВАЖКИХ ІОНІВ

С. Гаутам, Р. Кант

Резюме

Досліджено вплив кореляцій імпульсів на властивості фрагментів з легкими та середніми масами при введенні обрізання по імпульсах і кластеризації фазового простору. Проаналізовано розподіл швидкостей, $dN/p_t dp_t$ спектри, і відношення поздовжньої та поперечної енергій (E_{rat}) для реакцій $^{12}\text{C}+^{12}\text{C}$ і $^{40}\text{Ca}+^{40}\text{Ca}$. Виявлено суттєвий вплив обрізання за імпульсами на властивості фрагментів. Результати розрахунків порівняно з експериментальними даними.